

Measurement of the cross-section and forward-backward charge asymmetry for the b and c-quark in e^+e^- annihilation with inclusive muons at $\sqrt{s} = 58$ GeV

TOPAZ Collaboration

Y. Inoue¹, A. Miyamoto², E. Nakano¹, T. Takahashi¹, T. Tauchi², Y. Teramoto¹, K. Abe³, T. Abe^{3,1}, I. Adachi², K. Adachi⁴, M. Aoki³, M. Aoki⁵, R. Enomoto^{2,2}, K. Emi², H. Fujii², K. Fujii², T. Fujii^{6,9}, J. Fujimoto², N. Fujiwara⁴, H. Hirano⁵, B. Howell⁷, H. Hayashii⁴, N. Iida², H. Ikeda², S. Itami³, R. Itoh², H. Iwasaki², M. Iwasaki^{4,3}, R. Kajikawa³, K. Kaneyuki⁵, S. Kato², S. Kawabata², H. Kichimi², M. Kobayashi², D. Koltick⁷, I. Levine⁷, H. Mamada⁸, K. Miyabayashi⁴, K. Muramatsu⁴, K. Nagai^{9,4}, K. Nakabayashi³, M. Nakamura¹, S. Noguchi⁴, O. Nitoh⁸, A. Ochi⁵, F. Ochiai¹⁰, N. Ohishi³, Y. Ohnishi², Y. Ohshima⁵, H. Okuno², T. Okusawa¹¹, E. Shibata⁷, A. Sugiyama³, H. Sugiyama⁴, S. Suzuki³, K. Takahashi², T. Tanimori^{5,5}, M. Tomoto³, T. Tsukamoto², T. Tsumura⁸, S. Uno², Y. Watanabe⁵, A. Yamamoto², and M. Yamauchi²

¹*Institute for Cosmic Ray Physics, Osaka City University, Osaka 558-8585, Japan*

²*KEK, High Energy Accelerator Research Organization, Tsukuba, Ibaraki 305-0801, Japan*

³*Department of Physics, Nagoya University, Nagoya 464-8601, Japan*

⁴*Department of Physics, Nara Women's University, Nara 630-8506, Japan*

⁵*Department of Physics, Tokyo Institute of Technology, Tokyo 152-8551, Japan*

⁶*Department of Physics, University of Tokyo, Tokyo 113-0033, Japan*

⁷*Department of Physics, Purdue University, West Lafayette, IN 47907, USA*

⁸*Department of Applied Physics, Tokyo University of Agriculture and Technology, Tokyo 184-8588, Japan*

⁹*Department of Physics, The Graduate School of Science and Technology, Kobe University, Kobe 657-8501, Japan*

¹⁰*Department of Physics, Faculty of Liberal Arts, Tezukayama Gakuin University, Nara 631, Japan*

¹¹*Department of Physics, Osaka City University, Osaka 558-8585, Japan*

Abstract

We have studied inclusive muon events using all the data collected by the TOPAZ detector at $\sqrt{s} = 58$ GeV with an integrated luminosity of 273pb^{-1} . From 1328 inclusive muon events, we measured the ratio $R_{q\bar{q}}$ of the cross section for $q\bar{q}$ production to the total hadronic cross section and forward-backward asymmetry A_{FB}^q for b and c quarks. The obtained results are $R_{b\bar{b}} = 0.13 \pm 0.02(\text{stat}) \pm 0.01(\text{syst})$, $R_{c\bar{c}} = 0.36 \pm 0.05(\text{stat}) \pm 0.05(\text{syst})$, $A_{FB}^b = -0.20 \pm 0.16(\text{stat}) \pm 0.01(\text{syst})$ and $A_{FB}^c = -0.17 \pm 0.14(\text{stat}) \pm 0.02(\text{syst})$, in fair agreement with a prediction of the standard model.

Key words: Forward-backward asymmetry; b-quark; electron-positron

PACS: 13.65.+i, 13.10.+q

¹Present address: Stanford Linear Accelerator Center, Stanford University, Stanford, California 94309, U.S.A.

²Present address: Institute for Cosmic Ray Research, University of Tokyo, Chiba 277-8582, Japan

³Present address: University of Oregon, Eugene, OR 97403, U.S.A.

⁴Present address: Queen Mary and Westfield College, University of London, London, E1 4NS, UK

⁵Present address: Department of Physics, Kyoto University, Kyoto 606-8502, Japan

1 Introduction

The $e^+e^- \rightarrow q\bar{q}$ cross section and charge asymmetry for heavy quarks (b and c quarks) are fundamental quantities of electroweak interactions. Especially, in the TRISTAN energy region, the maximum forward-backward charge asymmetry for quark pair production, predicted by the standard model, provides high sensitivity to quark couplings. In this paper, we report the final result of an analysis for the quark pair production cross-section ratio to the total hadronic cross-section ($R_{q\bar{q}}$) and forward-backward asymmetry of b and c-quark (A_{FB}), using the data of all the high-luminosity runs collected by the TOPAZ detector at the TRISTAN electron positron collider. The data were collected from 1990 to 1995 at $\sqrt{s} = 58$ GeV, corresponding to a total integrated luminosity of 273 pb^{-1} . Previously, by using parts of the TOPAZ data, we reported on measurements of the heavy quark production cross section and charge asymmetry: through inclusive muons(1), inclusive electrons(2; 3) and $D^{*\pm}$ (4). In the previous inclusive muon analysis, we derived the b-quark parameters assuming the standard-model parameters for the c-quark with 41 pb^{-1} of data. The obtained result was $A_{\text{FB}}^b = -0.71 \pm 0.34(\text{stat}) \begin{smallmatrix} +0.07 \\ -0.08 \end{smallmatrix}(\text{syst})(1)$. Through inclusive electrons, the results were $A_{\text{FB}}^c = -0.49 \pm 0.20(\text{stat}) \pm 0.08(\text{syst})$ and $A_{\text{FB}}^b = -0.64 \pm 0.35(\text{stat}) \pm 0.13(\text{syst})$, using 197 pb^{-1} of data(2). In this paper, we derive $R_{q\bar{q}}$ and A_{FB} for both the b- and c-quark using the inclusive muon events with improved statistics. Data samples in previous analyses are included. In addition, we perform a correction on the pion punch-through rate using the measured data of pions from τ pairs.

The paper is structured as follows. A description of the TOPAZ detector and an overview of the data taking are given in Section 2. The hadronic event selection and the muon identification are described in Section 3. Section 4 describes the analysis, including a Monte-Carlo simulation, flavor separation, fitting method, and systematic uncertainty of the measured parameters. Section 5 presents discussions of the fitting results and shows some figures compared to the other experimental results. Finally, conclusions are given in Section 6.

2 Detector and data taking

2.1 TOPAZ detector

TOPAZ detector was a general-purpose 4π detector located at the TSUKUBA experimental hall. A quadrant cross section of the TOPAZ detector is shown in Figure 1. The detector was upgraded in time for the high-luminosity runs which started in 1990. The upgrade was done by adding a vertex chamber, a ring calorimeter and forward-backward muon chambers; further, the inner drift chamber was replaced by a trigger chamber, and the luminosity monitor was replaced by a forward calorimeter. After the upgrade, tracking of charged particle was done by a vertex chamber (VTX) (5), a trigger chamber (TCH) and a time projection chamber (TPC)(6), which were placed inside of a 1T magnetic field, produced by a super-conducting solenoid magnet (SCS)(7). Time-of-flight counters (TOF) (8) placed inside of SCS were used to provide information about the time-of-flight and trigger. The energies of electrons and photons were detected with a barrel calorimeter (BCL)(9), a ring calorimeter (RCL), an endcap calorimeter (ECL)(10; 11) and a forward calorimeter (FCL)(12). Those calorimeters were installed outside of the tracking devices. The total angular coverage of these calorimeters was $|\cos\theta| < 0.998$. The muon detection system (MDC)(13) consisted of the barrel part and the forward-backward part. They were placed at the outermost part of the TOPAZ detector. The coordinate system used was: z for the direction of the electron beam, θ for the polar angle measured from the z axis, ϕ for the azimuth angle measured from the horizontal direction pointing to the outward direction of the accelerator ring and r for the radial direction from the beam axis. In this analysis, we mainly used TPC, BCL, ECL and

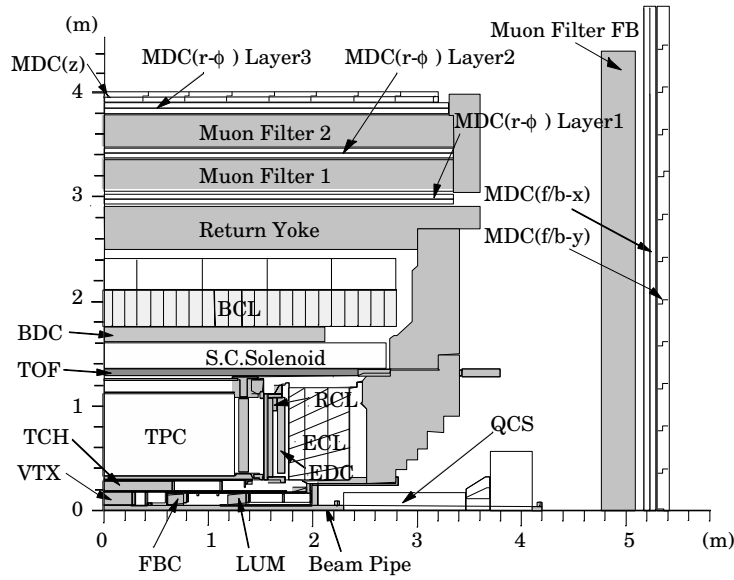


Figure 1: Quadrant cross section of the TOPAZ detector.

MDC.

Time projection chamber (TPC) The Time Projection Chamber (TPC) was the central tracking device. Its function was to measure the 3-dimensional positions and dE/dX of charged particles. The inner and outer radii of the TPC were 36 cm and 109 cm, respectively, and its length was 260 cm. Its polar angle coverage was $|\cos\theta| < 0.83$. They were made of 8 sectors divided into the forward and backward side, separated by a central membrane. The detection of drifted electrons was performed by 16 multiwire proportional chambers, placed on the end plane of each sector. The chamber was filled with an $\text{Ar}/\text{CH}_4 = 90/10$ mixture gas (P10) at 3.5 atm. The momentum resolution of TPC was $\sigma_{p_T}/p_T = \sqrt{(1.5p_T(\text{GeV}/c))^2 + (1.6)^2}\%$.

Electromagnetic calorimeter (BCL and ECL) The barrel calorimeter (BCL) was made of 4,300 lead glass blocks with photo-multipliers. Each lead glass block had a 20 radiation length. Its polar-angle coverage was $|\cos\theta| < 0.84$. The BCL energy resolution was $\sigma_E/E = \sqrt{(8.0)^2/E(\text{GeV}) + (2.5)^2}\%$, measured by Bhabha events.

The endcap calorimeter (ECL) was a pair of sampling gas calorimeters, and it consisted of a sandwich of conductive plastic tubes with cathode readouts and 2 or 3 mm thick lead plates. The total radiation length of the detector was 18. Its coverage was $0.85 < |\cos\theta| < 0.98$. The energy resolution of ECL was $\sigma_E/E = 6.7\%$ for Bhabha events.

Muon drift chamber (MDC) The muon detector (MDC) consisted of a barrel part (BMU) and a forward-backward part (EMU). In the present analysis, we only used BMU. BMU was located outside of the return yoke, which was made of 40 cm thick steel. BMU consisted of 3 superlayers of muon chambers interleaved with 2 layers of 30 cm thick muon filters made of steel. Each superlayer had double-layers of drift chambers, both measuring the ϕ direction of the track. In the outermost superlayer, we had an extra double-layer of drift chambers that measured the z direction of the track. The polar-angle coverage of BMU was $|\cos\theta| < 0.66$, and the minimum absorption length of BMU was 7.9. The muon drift chambers were made of extruded aluminum tube modules. One module contained eight cells, each 10 cm wide and 5 cm high, arranged in two layers of four cells each, staggered by a half cell to cover the dead regions near the cell walls. The averaged detection efficiency of each plane was 96%, measured using cosmic rays.

Trigger system The main triggers were made of an energy trigger, a track trigger and a muon trigger(14; 15; 16). The majority of the hadronic events were triggered by the energy trigger. The energy trigger required one of the following four conditions to be satisfied: 1) The total energy deposited in BCL be greater than 2 or 4 GeV, depending on the run conditions, or 2) the sum of the energy in the forward and backward ECL detectors be greater than 10 GeV, or 3) the BCL system had two energy clusters, both greater than 1 GeV, or 4) there were no energy clusters of energy greater than 3 GeV in neither the forward nor the backward ECL. The rate of energy triggering was approximately 1 Hz.

The track trigger required that there be at least 2 tracks having an opening angle larger than 45° in the $r - \phi$ plane. Their vertex position was required to be within ± 20 cm of the interaction point along the beam direction by a software trigger.

The muon trigger system was implemented for triggering $e^+e^- \rightarrow \mu^+\mu^-$ events in high-luminosity runs. Muon track signals were made of 8-OR signals of BMU drift tubes in coincidence with TOF signals. The muon trigger required two muon track signals. The opening angle of two tracks was required to be greater than 135° .

2.2 Data taking

TOPAZ started data taking in the spring of 1987 and ended in the summer of 1995. The total integrated luminosity was 340pb^{-1} . In 1990, the TRISTAN main ring was upgraded so as to increase the luminosity. Then, the collision energy was fixed at 58 GeV to maximize the luminosity. The data used in this analysis were taken at $\sqrt{s} = 58$ GeV during the period given in Table 1. The data before 1990 and the data in January 1993 were not used because the beam energy was not 29 GeV. The data in the first quarter of 1995 were not used because of a detector problem.

Table 1: Event sample.

| Period | integrated luminosity (pb^{-1}) | No. of Hadronic events |
|---------------------|--|------------------------|
| Feb, 1990~Dec, 1992 | 114 | 12,811 |
| Feb, 1993~Dec, 1994 | 144 | 14,942 |
| Apr, 1995~May, 1995 | 15 | 1,808 |
| | 273 | 29,561 |

3 Inclusive muon selection

3.1 Hadronic event selection

To select inclusive muon events, we first selected hadronic events from DSTs using the TOPAZ standard selection criteria for hadronic events (17), which were:

- (1) At least five “good” tracks were coming from the interaction point, where a “good” track was defined by (i) $r < 5$ cm and $|z| < 5$ cm at the closest point of approach to the beam axis, (ii) $p_T > 0.15$ GeV/c, and (iii) $|\cos\theta| < 0.83$.
- (2) The total visible energy, E_{vis} , had to exceed the beam energy, E_{beam} .
- (3) The momentum balance, $|\sum p_z|/E_{vis}$, was less than 0.4.
- (4) The larger of the invariant jet masses in the two hemispheres, divided by the plane perpendicular to the thrust axis, M_{jet} , exceeded 2.5 GeV/ c^2 .
- (5) The number of clusters having an energy greater than $E_{beam}/2$ was less than 2.

The background processes for the hadronic events were mainly τ pairs and two-photon events. Especially, τ pairs have a 17% branching ratio for decaying into muons, and have a large forward-backward asymmetry; hence, it could cause a significant background to the asymmetry measurement. To reduce these backgrounds, we required additional tight selection criteria, which were:

- At least two charged tracks existed in each hemisphere.
- A tighter cut on the invariant jet mass in the criteria(4): $M_{jet} > 3.5$ GeV/ c^2 .

A total of 29,561 events passed the above requirements. Using Monte-Carlo simulations, we determined the efficiency of this hadronic event selection to be $65.08 \pm 0.07\%$ (systematic error only). The remaining background in the selected events were estimated to be 0.2% from τ pairs and 0.1% from two-photon events, according to a Monte-Carlo study (18; 19). These are negligible, compared with the statistical errors and the other systematic errors in this analysis. Out of this hadronic event sample we excluded those events that had no high voltage on MDC. After this selection, 27,614 hadronic events remained.

3.2 Muon identification

Muon identification in hadronic events suffered from fake muons, such as punch-throughs and decay-in-flights of hadrons. In order to discriminate prompt muons from fake muons, following criteria were employed:

- (i) The track had to pass the “good” track cuts, described in the previous subsection.
- (ii) The momentum of the track had to be greater than 2.5 GeV/c and $|\cos\theta| < 0.6$.

After the track passed (i) and (ii), the track was extrapolated to MDC, assuming that it was a muon. We then applied the following.

- (iii) All three $r - \phi$ superlayers of MDC had to have at least one hit in each superlayer within 20 cm or $3\sigma_{track}$ from the extrapolated tracks. Here, σ_{track}^2 is the quadratic sum of the track extrapolation errors, the multiple Coulomb scattering errors, detector space resolution, and the error due to the detector alignment. In addition, we required that at least one superlayer had to have adjacent firing cells in the other layer of the same superlayer.
- (iv) MDC hits were not allowed to be shared by the other tracks.

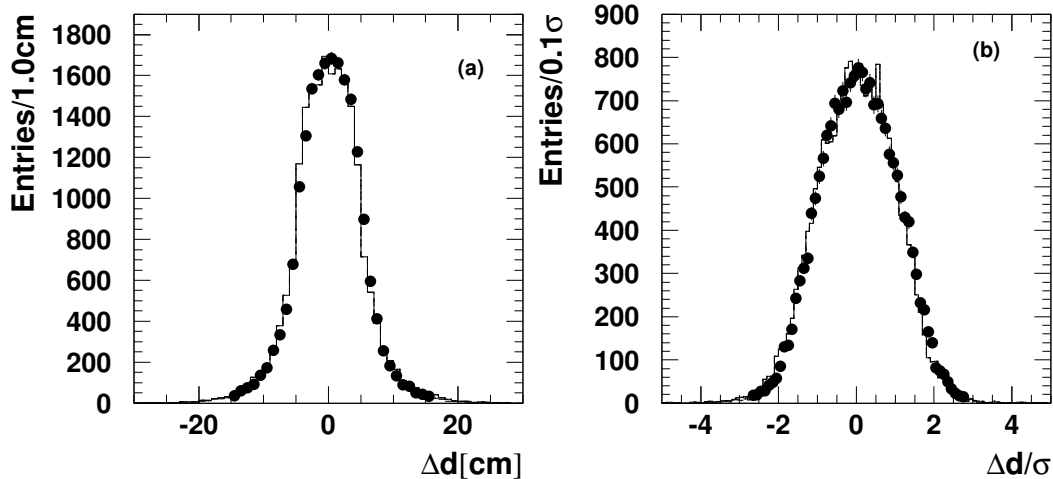


Figure 2: Δd (a) and $\Delta d/\sigma_{track}$ (b) for muons. The dots with error bars are cosmic-ray data. Histograms are Monte Carlo prediction.

The capability of the Monte-Carlo to simulate muons has been tested with cosmic-ray muons. Figure 2 shows the distance between the extrapolated track and the associated hit, Δd , and $\Delta d/\sigma_{track}$. As can be seen in these figures, the Monte-Carlo simulation and the data are in good agreement. The muon identification efficiencies as a function of momentum p and also as a function of $\cos\theta$ are shown in Figure 3. The efficiency shows a plateau over 2.5 GeV/c in p and $|\cos\theta| < 0.6$. The measured efficiency for muon identification is 93% at the plateau, which agrees with the Monte-Carlo prediction within 1%. The inefficiency was due to dead wires in MDC (3%), dead regions in the sector boundaries (3%) and cuts on the distance between the MDC hits and the track (1%).

The number of inclusive muon events was 1,328, after selecting the hadronic events by muon identification. If an event had two or more muon candidates, we chose the one with the highest momentum as the muon for tagging c and b quarks.

4 Analysis

4.1 Monte Carlo simulation

We used JETSET7.3(20) for $e^+e^- \rightarrow q\bar{q}$ event generations. The used parameters in JETSET7.3 were tuned-up for hadronic events using the event shape data (21). In the hadronization, we used the LUND symmetric function for the fragmentation function for light quarks (u,d,s) with $a = 0.413$ and $b = 0.9$. For heavy quarks (c,b), a function by Peterson *et al.*(22) was used with $\epsilon_c = 0.05$ and $\epsilon_b = 0.01$. For the standard model parameters, we used $\sin^2\theta_W = 0.2315$, $M_{Z^0} = 91.187$ GeV/c², and $\Gamma_{Z^0} = 2.490$ GeV(23).

For a detector simulation, we used the TOPAZ detector simulator, which simulated the be-

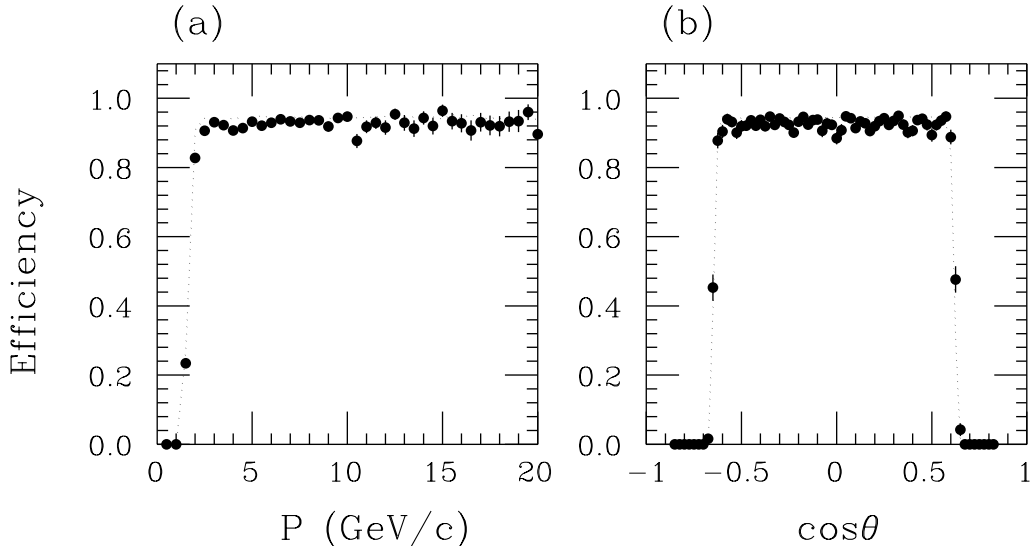


Figure 3: Muon identification efficiency measured through cosmic-ray muons (dot with error bars) and Monte-Carlo prediction (dotted line) as a function of the momentum (a) and polar angle (b).

haviors of the particles in the TOPAZ detector: such as the energy loss, multiple scattering, decay-in-flights and the detector signals. For the simulations of particle's interactions with the detector material, EGS4(24) was used for electromagnetic processes and GHEISHA-7(25) for nuclear interactions. We used 314,463 hadronic events for the studies described in this paper.

To test the validity of the hadronic event selection and the Monte-Carlo simulation, we examined the general features of hadronic events. Figure 4 shows the distributions of the momentum (a) and the polar angle (b) of the track, and the polar angle of the thrust axis (c). The data and the Monte-Carlo results are in good agreement, except for a dip observed at $\theta = 90^\circ$ in the polar-angle distribution. This dip is due to the effect of the central membrane of TPC. The track reconstruction inefficiency at the membrane is 0.4% for hadronic events and 0.8% for inclusive muon events. The effect of this inefficiency is negligible on the cross section and asymmetry results.

4.2 Background estimation

Possible background sources to prompt muons are hadron punch-throughs, muons from decay-in-flights of light hadrons (mainly π^\pm and K^\pm) and accidental hits in MDC due to the beam backgrounds or cosmic rays. To estimate the rate of accidental hits, we applied the muon identification criteria to the electron (positron) tracks in Bhabha events, obtained in the same experimental period. No track was identified as a muon. From this result, the accidental hit rate was considered to be negligible.

The other background sources were evaluated using Monte-Carlo simulations. Since the pion and kaon lifetimes and decay modes are well established, the decay-in-flights of light hadrons can be precisely calculated in the simulation. On the other hand, the rate of hadron punch-throughs depends on nuclear interactions with detector materials. Therefore, it must be verified

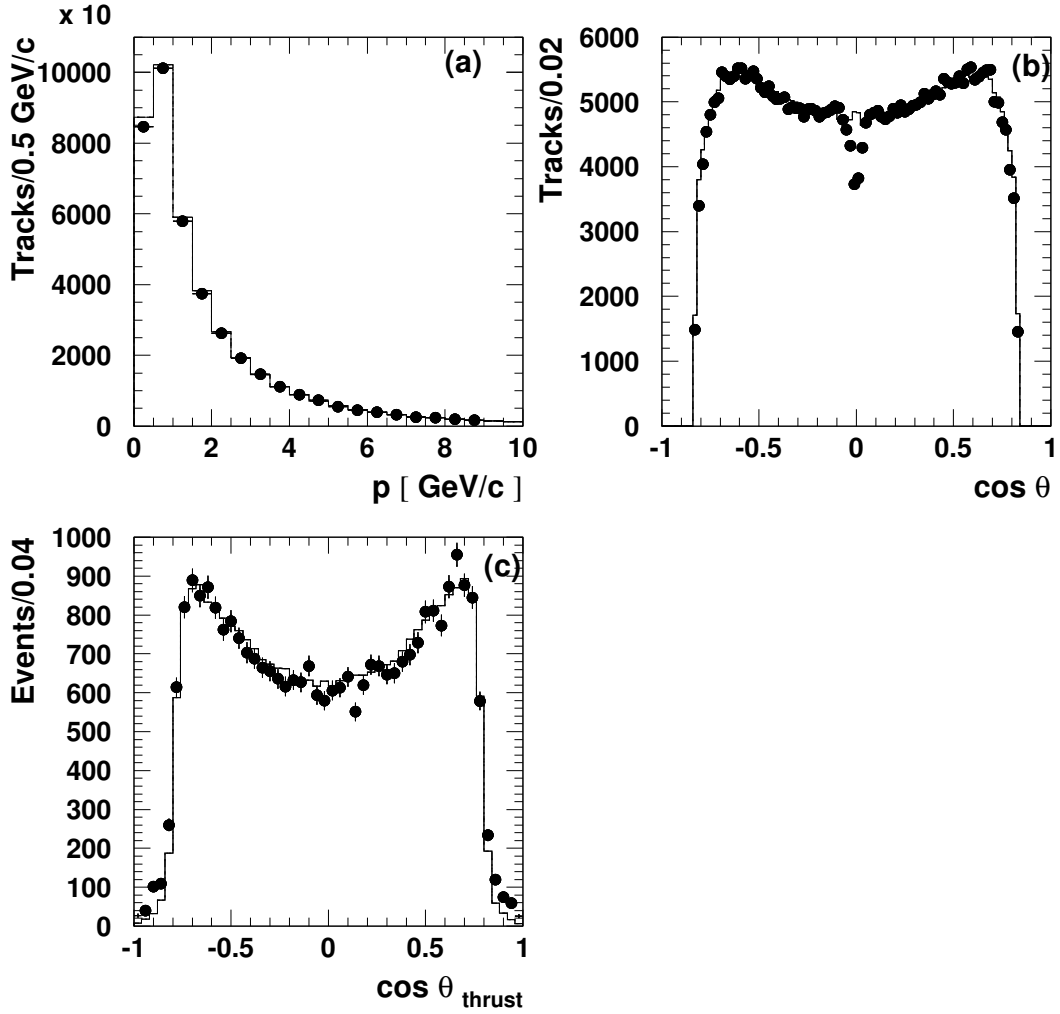


Figure 4: Hadronic events; momentum (a) and polar angle (b) of good tracks, and angular distribution of thrust axis (c). The dots with error bars are the data; the histograms are Monte-Carlo results.

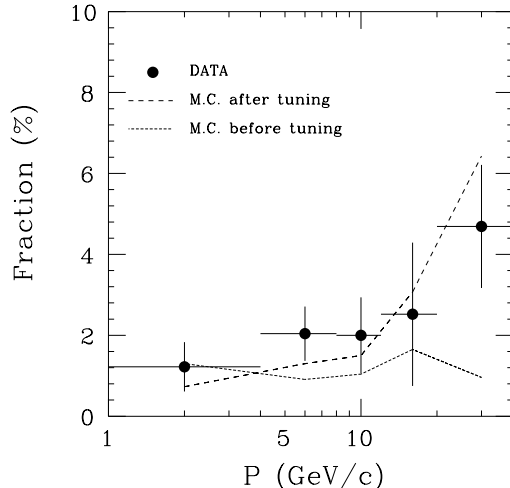


Figure 5: Punch-through rate as a function of momentum derived through the pions from τ -pairs. The dots with error bars are the data. The dotted and dashed lines are Monte Carlo simulations before and after tuning the parameters in GHEISHA.

experimentally. For this purpose, we studied the punch-through of pions by using 1,202 charged pions from $\tau \rightarrow \pi\pi\pi\nu$ and $\tau \rightarrow \rho\nu \rightarrow \pi^\pm\pi^0\nu$ in the $e^+e^- \rightarrow \tau^+\tau^-$ events. Figure 5 shows the experimental ratio together with the Monte-Carlo expectation as a function of the momentum. As can be clearly seen in this figure, it was found that the Monte-Carlo prediction significantly underestimated the rate, especially in the high-momentum region with the default parameters. To correct this difference, we tuned up the most influential parameter, which is the total cross section of pions (kaons) interacting with materials in the GHEISHA routine. We introduced a correction factor to scale the total cross section as a function of the momentum, as listed in Table 2. In the high-momentum region of $p > 10$ GeV/c, the correction factor was determined through the pion punch-through rate in the τ pair events. For $p < 3$ GeV/c, the correction factor was estimated through energy deposits of hadrons in BCL, and it was fitted to a function. These two correction factors were linearly connected in the intermediate momentum regions, i.e. $3 < p < 10$ GeV/c.

The results of the tuned-up Monte-Carlo simulation are also shown in Figure 5. The discrepancy between the Monte-Carlo results and the data was reduced significantly with the tuned-up Monte-Carlo procedure.

Table 2: Correction factor for the cross section for each momentum region.

| Momentum region (GeV/c) | correction factor $f(p)$ |
|-------------------------|-------------------------------------|
| $p < 3$ | $f(p) = -0.013p^2 + 0.139p + 0.826$ |
| $3 \leq p < 10$ | $f(p) = -0.054p + 1.295$ |
| $10 \leq p$ | $f(p) = 0.726$ |

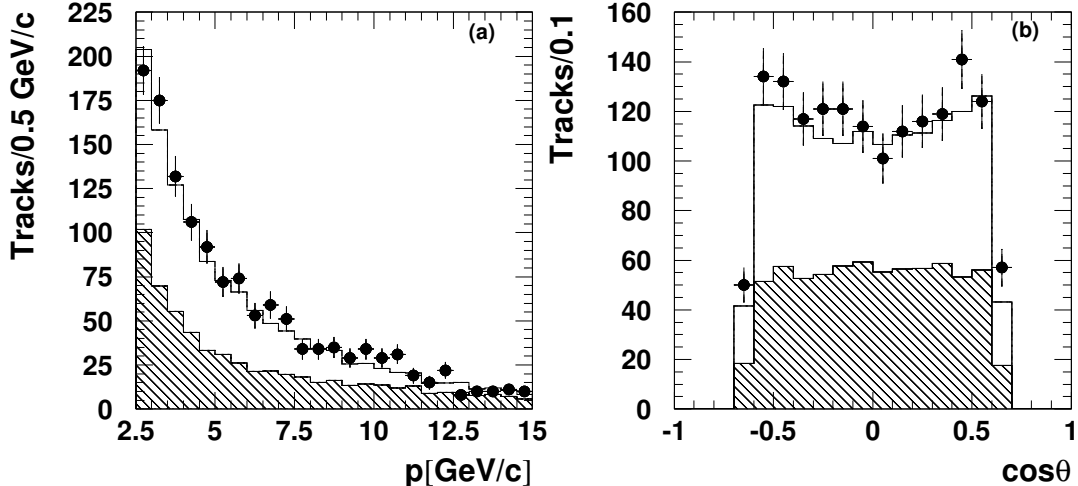


Figure 6: Distributions of momentum (a) and polar angle (b) of inclusive muons. The dots with error bars are data and the histograms are Monte-Carlo results. The open regions show the contributions from c and b quarks. The shaded regions are the background from light quarks.

In the inclusive muon sample, the fractions of decay-in-flight and hadron punch-through were estimated to be 25% and 23%, respectively, by using the tuned-up Monte-Carlo program. Figure 6 shows the momentum spectrum (a) and polar-angle distribution (b). The background from light quarks was obtained by a Monte-Carlo simulation using the total number of hadronic events for normalization.

4.3 Flavor separation

Inclusive muon events can be categorized into four groups by the sources: (A) prompt muons from primary b -decays ($b \rightarrow \mu$), (B) cascade muons from $b \rightarrow c(\bar{c})$ decays ($b \rightarrow c \rightarrow \mu$), (C) prompt muons from primary c -decays ($c \rightarrow \mu$), and (D) backgrounds from decay-in-flights and punch-throughs (*others*). In this analysis, we included the $b \rightarrow \tau \rightarrow \mu$ mode in category (A). Table 3 gives the results of Monte-Carlo studies, giving the fraction of each components in the inclusive muon events.

We used the thrust axis to determine the primary quark direction. The accuracy of the quark direction determined by this method was estimated to be 5° , based on a study by a Monte-Carlo simulation. We define the angle of the quark direction by $-Q \cos \theta_{trust}$, where Q is the charge of the tagged muon and θ is the angle of the thrust axis with respect to the beam axis. To separate the quark flavors, we used the muon transverse momentum with respect to the jet axis, p_T^{jet} . Jets were reconstructed using the JADE jet clustering algorithm(26) with a scaled invariant mass cut, $Y_{cut}(= M_{ij}/E_{vis}) = 0.04$. Muons from b -quarks have a larger p_T^{jet} compared with those from c -quarks, due to the heavy b -quark mass. Using the p_T^{jet} cut at 0.8 GeV/c, we classified the inclusive muon events into a b -enriched sample ($p_T^{jet} \geq 0.8$ GeV/c) and a c -enriched sample

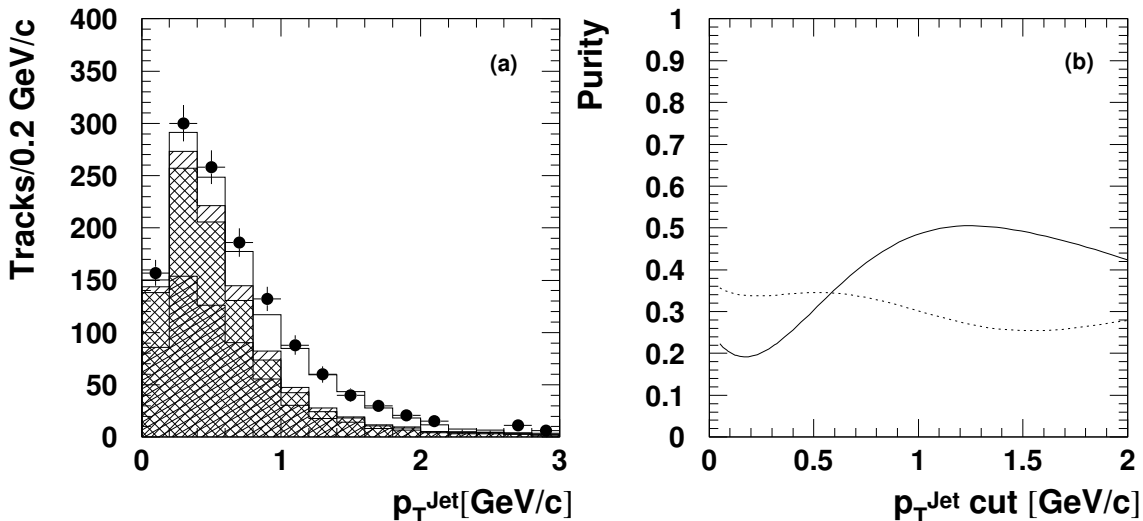


Figure 7: p_T^{jet} distribution of inclusive muons (a) and purities of b and c-quarks as a function of p_T^{jet} cut (b). In (a), dots with errors show the data. Histograms are Monte Carlo: $b \rightarrow \mu$ (open), $b \rightarrow c \rightarrow \mu$ (hatched), $c \rightarrow \mu$ (double-hatched) and *others*(triple-hatched), respectively. In (b), solid curve shows the b-quark purity and dotted curve shows the c-quark purity.

($p_T^{jet} < 0.8$ GeV/c). We chose $p_T^{jet} = 0.8$ GeV/c, because the systematic uncertainty was the smallest at 0.8 GeV/c. The purity of the c- and b-quarks as a function of the p_T cut was studied by a Monte-Carlo simulation. Figure 7 shows the b, c-quark purities as a function of the p_T cut. For b-quarks, the purity was calculated by summing up all of the b-quarks with p_T greater than a given p_T cut, divided by the total number of inclusive muon tracks in the same p_T region. For c-quarks, summing was done for p_T less than a given p_T cut.

Table 3: Percentage of muons from each source in the inclusive muon sample.

| Source | Fraction(%) | | total |
|-----------------------------------|-------------------------|----------------------------|-------|
| | $p_T^{jet} < 0.8$ GeV/c | $p_T^{jet} \geq 0.8$ GeV/c | |
| $b \rightarrow \mu$ | 9.7 | 41.9 | 20.1 |
| $b \rightarrow c \rightarrow \mu$ | 5.8 | 5.2 | 5.6 |
| $c \rightarrow \mu$ | 31.6 | 13.2 | 25.7 |
| <i>others</i> | 52.8 | 39.6 | 48.5 |

4.4 Simultaneous fit for b and c-quark

In a previous paper(1), we derived only the b-quark parameters by assuming the standard-model parameters for the c-quark because of low statistics. This time, we performed a four-parameter fit of $(R_{b\bar{b}}, R_{c\bar{c}}, A_{FB}^b, A_{FB}^c)$ to p and $-Q \cos \theta_{thrust}$ ($p_T^{jet} \geq 0.8$ GeV/c and < 0.8 GeV/c) distributions. Definitions of $R_{q\bar{q}}$, and A_{FB} are given by

$$R_{q\bar{q}} \equiv \sigma(e^+e^- \rightarrow q\bar{q})/\sigma(e^+e^- \rightarrow hadrons) \quad (1)$$

and

$$A_{FB} \equiv \frac{\sigma_F - \sigma_B}{\sigma_F + \sigma_B} \quad (2)$$

where σ represents the lowest order ($SU(3) \times SU(2)_L \times U(1)$) cross-section and $\sigma_F(\sigma_B)$ is the cross-section for quark to travel forward (backward) with respect to the e^- direction. The χ^2 of the fit was defined by

$$\begin{aligned} \chi_{total}^2 &= \chi_{\cos\theta(p_T^{jet} \geq 0.8 GeV/c)}^2 + \chi_{\cos\theta(p_T^{jet} < 0.8 GeV/c)}^2 + \chi_p^2 \\ &= \sum_{i=1}^8 \frac{(N_i^\mu - \tilde{N}_i^\mu)^2}{\sigma_{N_i^\mu}^2} + \sum_{j=1}^8 \frac{(N_j^\mu - \tilde{N}_j^\mu)^2}{\sigma_{N_j^\mu}^2} + \sum_{k=1}^6 \frac{(N_k^\mu - \tilde{N}_k^\mu)^2}{\sigma_{N_k^\mu}^2}, \end{aligned} \quad (3)$$

where N_i^μ and $\sigma_{N_i^\mu}$ are the number of inclusive muon events and the statistical error for each bin, respectively. \tilde{N}_i^μ is the number of expected events for each bin, which is defined by

$$\begin{aligned} \tilde{N}_i^\mu &= N_{had}^{exp} \{ R_{b\bar{b}} \cdot 2Br^{\text{sum}}(b \rightarrow \mu) F(A_{FB}^b)_i \cdot C_i^{b \rightarrow \mu} \\ &\quad + R_{b\bar{b}} \cdot 2Br(c \rightarrow \mu)(1 + \alpha) F(-\frac{1-\alpha}{1+\alpha} A_{FB}^b)_i \cdot C_i^{b \rightarrow c \rightarrow \mu} \\ &\quad + R_{c\bar{c}} \cdot 2Br(c \rightarrow \mu) F(-A_{FB}^c)_i \cdot C_i^{c \rightarrow \mu} \} \\ &\quad + N_i^{others} \end{aligned} \quad (4)$$

for $-Q \cos\theta_{thrust}$ bins, and

$$\begin{aligned} \tilde{N}_k^\mu &= N_{had}^{exp} \{ R_{b\bar{b}} \cdot 2Br^{\text{sum}}(b \rightarrow \mu) \cdot W_k^{b \rightarrow \mu} \\ &\quad + R_{b\bar{b}} \cdot 2Br(c \rightarrow \mu)(1 + \alpha) \cdot W_k^{b \rightarrow c \rightarrow \mu} \\ &\quad + R_{c\bar{c}} \cdot 2Br(c \rightarrow \mu) \cdot W_k^{c \rightarrow \mu} \} \\ &\quad + N_k^{others} \end{aligned} \quad (5)$$

for p bins, where N_{had}^{exp} is the total number of hadronic events. $Br^{\text{sum}}(b \rightarrow \mu)$ is the combined branching ratio of $Br(b \rightarrow \mu)$ and $Br(b \rightarrow \tau \rightarrow \mu)$. $Br(b \rightarrow \mu)$ and $Br(c \rightarrow \mu)$ are the branching ratios of $b \rightarrow \mu$ and $c \rightarrow \mu$, which are equivalent to the branching ratios for muons semileptonically decayed from b and c hadrons, respectively. $Br(b \rightarrow c\bar{c}s)$ is denoted as α in the above equations. The used branching ratios are listed in Table 4. $F(A_{FB}^q)_i$ is the polar-angle distribution function, integrated in each $\cos\theta$ bin (i -th bin), which is written as

$$F(A_{FB}^q)_i = \int_i \frac{3}{8} (1 + \cos^2\theta + \frac{8}{3} A_{FB}^q \cos\theta) d\cos\theta. \quad (6)$$

C_i^{mode} is the correction factor for the each $\cos\theta$ bin from the *decay mode*, given by

$$C_i^{mode} = \frac{(1 + \delta)_i^{q\bar{q}}}{(1 + \delta)_{total}^{had}} \frac{\eta_i^{q\bar{q}}}{\eta^{had}} \varepsilon_i^\mu, \quad (7)$$

where $(1 + \delta)_i^{q\bar{q}}$ is the combined correction factor of the QED (initial state photon radiation) and QCD (parton shower) radiative corrections for the i -th bin of $e^+e^- \rightarrow q\bar{q}$. Similarly, $(1 + \delta)_{total}^{had}$ is a radiative correction factor for the total hadronic cross section. These correction factors were estimated through a Monte-Carlo simulation based on the LUND event generator, JETSET7.3. $\eta_i^{q\bar{q}}$ is the acceptance correction for the i -th bin of each mode, η^{had} is that for hadronic events,

Table 4: Branching ratios used in the fits.

| Mode | Branching ratio(%) |
|--|--------------------|
| $Br^{\text{sum}}(b \rightarrow \mu)$ | 11.3 ± 0.5 |
| $Br(b \rightarrow \mu)(27)$ | 10.8 ± 0.5 |
| $Br(b \rightarrow \tau \rightarrow \mu)(28)$ | 0.45 |
| $Br(c \rightarrow \mu)(29)$ | 9.0 ± 0.7 |
| $Br(b \rightarrow c\bar{c}s)(30)$ | 21.9 ± 3.7 |

and ε_i^μ is the muon identification efficiency for the i -th bin ($\cos\theta$ bin). W_k^{mode} is the correction factor for each p bin, which is given by

$$W_k^{mode} = \frac{(1 + \delta)_k^{q\bar{q}}}{(1 + \delta)_{total}^{had}} \frac{\eta_{k,mode}^{q\bar{q}}}{\eta^{had}} \varepsilon_k^\mu. \quad (8)$$

Table 5 gives the correction factors for each bin. N_i^{others} is the number of background events for the i -th bin, which is also listed in Table 5. The numbers were derived through Monte Carlo simulations.

As a result of the four-parameter fit (Figure 8 and 9), we obtained $R_{b\bar{b}} = 0.13 \pm 0.02$, $R_{c\bar{c}} = 0.36 \pm 0.05$, $A_{FB}^b = -0.20 \pm 0.16$ and $A_{FB}^c = -0.17 \pm 0.14$, with $\chi^2/\text{D.O.F} = 14.93/18$. The errors are statistical only. The correlation coefficients obtained from the fit is given in Table 6. The 1σ contours of the fit for R_{cc} v.s. R_{bb} and A_c v.s. A_b are shown in Figure 9.

4.5 Systematic errors for $R_{q\bar{q}}$ and A_{FB}^q

Possible sources of systematic errors are listed in Table 7. The largest systematic error comes from the uncertainty in the probabilities of mis-identified hadrons as muons. This is caused by the light quark background in the heavy quark samples. In order to estimate the effect of hadron mis-identifications, we performed the same analysis by changing the correction factor of the effective pion-nucleus cross section by $\pm 1\sigma$ of the measured error of fake rate. The effect of the cuts on muon identification was studied by varying the cut values on momentum p , Δd , and $\Delta d/\sigma_{track}$ by ± 0.5 GeV/c, ± 5 cm, and $\pm 0.5\sigma_{track}$, respectively, and examined the change in the obtained cross sections and asymmetries. We studied the effect of the p_T^{jet} cut by shifting the cut value by ± 0.1 GeV/c. The effect of the uncertainty in the MDC detector acceptance was checked by varying the $|\cos\theta_{track}|$ cut from 0.6 to 0.58. Based on these studies, we selected the cut values that minimize the systematic errors. The error due to the semileptonic branching ratios for b and c hadrons were obtained by changing the branching ratios by $\pm 1\sigma$ of the quoted number. Changes of fragmentation parameters cause the changes in the muon identification efficiency and flavor separation. The error due to this effect was estimated by changing the fragmentation parameters by $\pm 1\sigma$ of the quoted number.

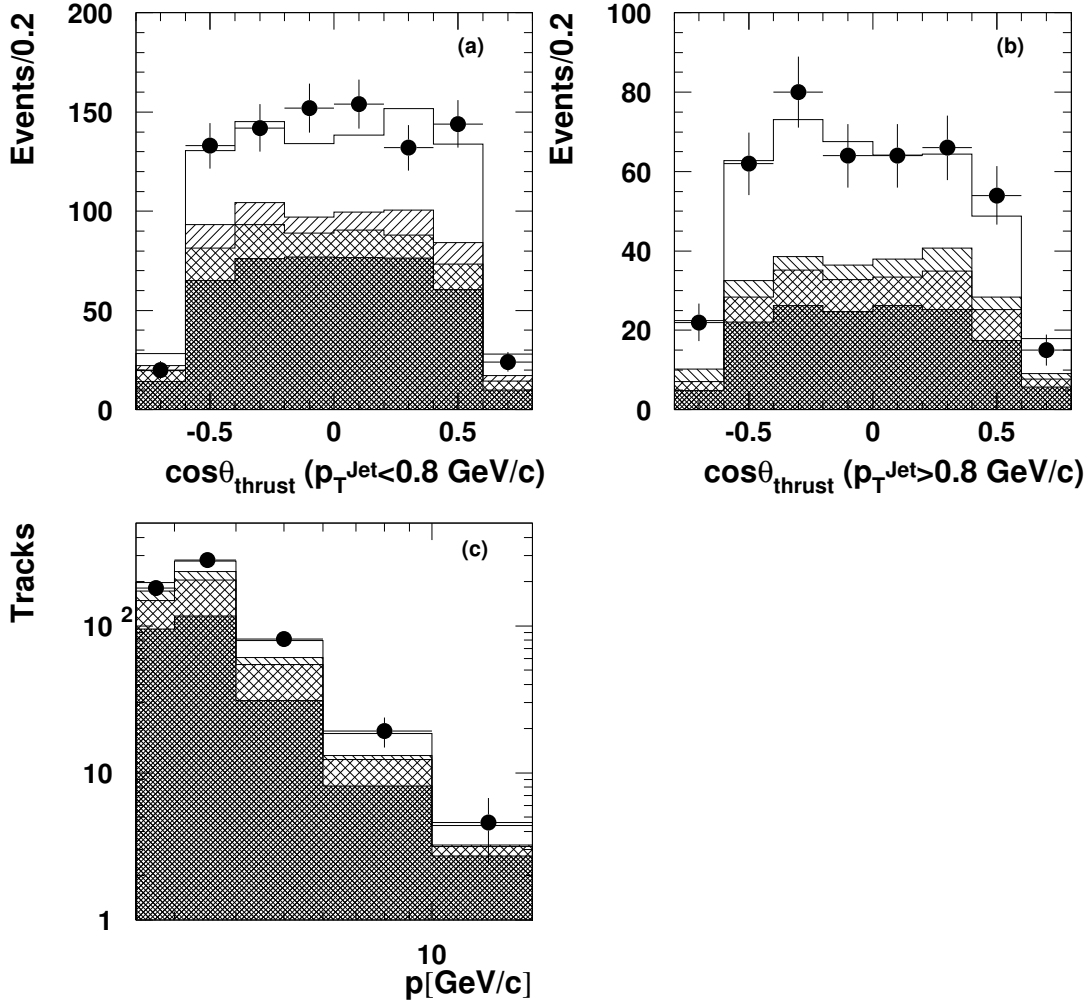


Figure 8: Results of the four-parameter fit: $\cos\theta_{thrust}$ for the c-enriched sample ($p_T^{jet} < 0.8$ GeV/c) (a) and the b-enriched sample ($p_T^{jet} \geq 0.8$ GeV/c) (b), and momentum distributions (c). The dots with error bars are the data. The histograms are the results from the four-parameter fit: $b \rightarrow \mu$ (open), $b \rightarrow c \rightarrow \mu$ (hatched), $c \rightarrow \mu$ (double-hatched) and *others* (triple-hatched), respectively.

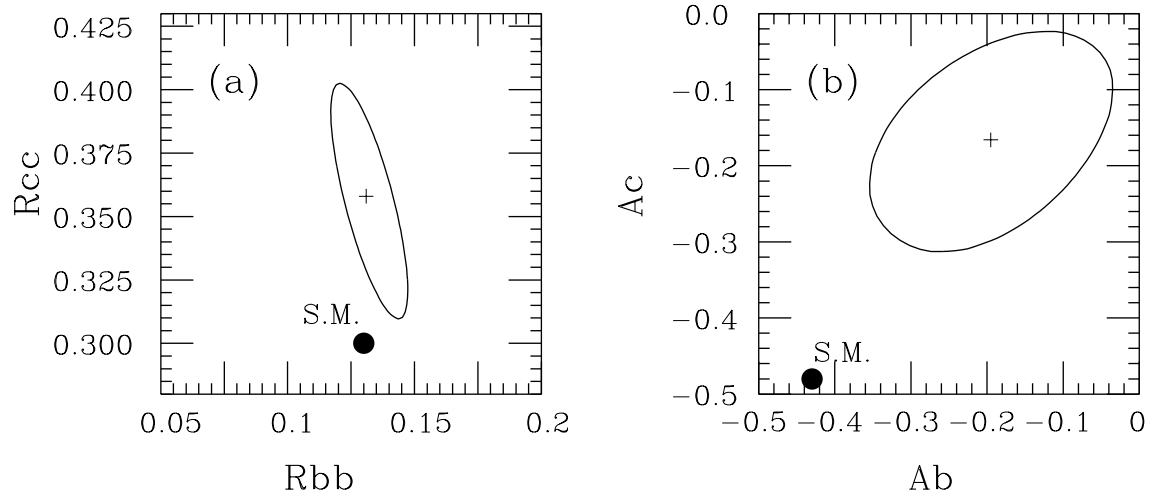


Figure 9: Results of the four-parameter fit for $R_{q\bar{q}}$ (a) and A_{FB}^q (b). The cross bar indicates the central value and the ellipse shows 1σ contour. The errors are only statistical. The points show the standard-model prediction.

Table 5: Number of events and correction factors in each bin.

(a) Correction factor for each $\cos\theta$ bin: $p_T^{Jet} < 0.8$ (GeV/c)

| $\cos\theta$ bin | N_i^μ | N_i^{others} | $C_i^{b\rightarrow\mu}$ | $C_i^{b\rightarrow b\rightarrow\mu}$ | $C_i^{c\rightarrow\mu}$ |
|------------------|-----------------|----------------|-------------------------|--------------------------------------|-------------------------|
| -0.8 \sim -0.6 | 20. \pm 4.5 | 14.0 \pm 1.1 | 0.049 | 0.034 | 0.038 |
| -0.6 \sim -0.4 | 133. \pm 11.5 | 65.0 \pm 2.4 | 0.178 | 0.180 | 0.271 |
| -0.4 \sim -0.2 | 142. \pm 11.9 | 76.2 \pm 2.6 | 0.222 | 0.187 | 0.319 |
| -0.2 \sim 0.0 | 152. \pm 12.3 | 76.9 \pm 2.6 | 0.183 | 0.137 | 0.288 |
| 0.0 \sim 0.2 | 154. \pm 12.4 | 76.6 \pm 2.6 | 0.234 | 0.149 | 0.273 |
| 0.2 \sim 0.4 | 132. \pm 11.5 | 76.5 \pm 2.6 | 0.201 | 0.176 | 0.313 |
| 0.4 \sim 0.6 | 144. \pm 12.0 | 60.5 \pm 2.3 | 0.209 | 0.128 | 0.253 |
| 0.6 \sim 0.8 | 24. \pm 4.9 | 9.8 \pm 0.9 | 0.064 | 0.029 | 0.044 |

(b) Correction factor for each $\cos\theta$ bin: $p_T^{Jet} \geq 0.8$ (GeV/c)

| $\cos\theta$ bin | N_i^μ | N_i^{others} | $C_i^{b\rightarrow\mu}$ | $C_i^{b\rightarrow c\rightarrow\mu}$ | $C_i^{c\rightarrow\mu}$ |
|------------------|---------------|----------------|-------------------------|--------------------------------------|-------------------------|
| -0.8 \sim -0.6 | 22. \pm 4.7 | 4.8 \pm 0.7 | 0.106 | 0.042 | 0.014 |
| -0.6 \sim -0.4 | 62. \pm 7.9 | 22.0 \pm 1.4 | 0.326 | 0.062 | 0.046 |
| -0.4 \sim -0.2 | 80. \pm 8.9 | 26.3 \pm 1.5 | 0.449 | 0.057 | 0.070 |
| -0.2 \sim 0.0 | 64. \pm 8.0 | 24.8 \pm 1.5 | 0.476 | 0.063 | 0.062 |
| 0.0 \sim 0.2 | 64. \pm 8.0 | 26.3 \pm 1.5 | 0.443 | 0.073 | 0.050 |
| 0.2 \sim 0.4 | 66. \pm 8.1 | 25.2 \pm 1.5 | 0.411 | 0.080 | 0.060 |
| 0.4 \sim 0.6 | 54. \pm 7.3 | 17.4 \pm 1.2 | 0.334 | 0.037 | 0.040 |
| 0.6 \sim 0.8 | 15. \pm 3.9 | 5.7 \pm 0.7 | 0.125 | 0.014 | 0.008 |

(c) Correction factor for each momentum bin

| Momentum bin (GeV/c) | N_k^μ | N_k^{others} | $W_k^{b\rightarrow\mu}$ | $W_k^{b\rightarrow c\rightarrow\mu}$ | $W_k^{c\rightarrow\mu}$ |
|----------------------|-----------------|-----------------|-------------------------|--------------------------------------|-------------------------|
| 2.5 \sim 3.0 | 181. \pm 13.5 | 95.0 \pm 2.9 | 3.048 | 2.902 | 2.998 |
| 3.0 \sim 4.0 | 281. \pm 16.7 | 116.9 \pm 3.2 | 4.921 | 3.764 | 4.903 |
| 4.0 \sim 6.0 | 325. \pm 18.0 | 124.6 \pm 3.3 | 4.572 | 1.573 | 2.627 |
| 6.0 \sim 10.0 | 309. \pm 17.6 | 130.5 \pm 3.4 | 2.600 | 0.402 | 0.936 |
| 10.0 \sim 16.0 | 165. \pm 12.8 | 98.2 \pm 2.9 | 0.865 | 0.045 | 0.145 |
| 16.0 \sim 30.0 | 68. \pm 8.2 | 43.2 \pm 1.9 | 0.091 | 0.007 | 0.017 |

Table 6: The correlation coefficients for the parameters in the four-parameter fit.

| | $R_{b\bar{b}}$ | $R_{c\bar{c}}$ | A_{FB}^b | A_{FB}^c |
|----------------|----------------|----------------|------------|------------|
| $R_{b\bar{b}}$ | 1 | -0.77 | 0.01 | -0.17 |
| $R_{c\bar{c}}$ | | 1 | -0.37 | 0.16 |
| A_{FB}^b | | | 1 | 0.44 |
| A_{FB}^c | | | | 1 |

Table 7: Summary of systematic errors

| Source | $\Delta R_{b\bar{b}}/R_{b\bar{b}}$ | $\Delta R_{c\bar{c}}/R_{c\bar{c}}$ | $\Delta A_{FB}^b/A_{FB}^b$ | $\Delta A_{FB}^c/A_{FB}^c$ |
|-------------------------|------------------------------------|------------------------------------|----------------------------|----------------------------|
| hadron mis-ID | 4.9% | 12.1% | 3.8% | 13.3% |
| muon ID | <0.1% | 0.6% | 1.5% | 0.9% |
| p_T^{jet} cut | 0.9% | 0.6% | 1.5% | 0.2% |
| MDC acceptance | <0.1% | <0.1% | 0.5% | 0.9% |
| branching ratio | 2.8% | 5.0% | 2.1% | 1.2% |
| fragmentation parameter | 1.7% | 3.8% | <0.1% | <0.1% |
| total | 6.1% | 13.7% | 4.9% | 13.8% |

5 Discussion

The results of the four-parameter fits with systematic errors are $R_{b\bar{b}} = 0.13 \pm 0.02(stat) \pm 0.01(syst)$, $R_{c\bar{c}} = 0.36 \pm 0.05(stat) \pm 0.05(syst)$, $A_{FB}^b = -0.20 \pm 0.16(stat) \pm 0.01(syst)$ and $A_{FB}^c = -0.17 \pm 0.14(stat) \pm 0.02(syst)$. Four-parameter fits of the c- and b-quark have correlations in the parameters of the c-quark and b-quark. For example, an increase of $R_{c\bar{c}}$ would cause $R_{b\bar{b}}$ to decrease. Also, an increase of A_{FB}^c would cause A_{FB}^b to increase. To estimate this effect, we applied one quark parameter fit, by fixing the other quark parameters to the standard-model predictions. The used values of the standard model parameters are $R_{b\bar{b}} = 0.13$, $A_{FB}^b = -0.43$ for the c-quark fit and $R_{c\bar{c}} = 0.30$, $A_{FB}^c = -0.48$ for the b-quark fit. For A_{FB}^b , correction for $B_{d,s}^0 B_{d,s}^0$ mixing is included using the mixing parameter at high energy, $\chi_B = 12\%$. The results of the fits are $R_{b\bar{b}} = 0.15 \pm 0.01$, $A_{FB}^b = -0.29 \pm 0.13$ (b-quark fit) and $R_{c\bar{c}} = 0.36 \pm 0.03$, $A_{FB}^c = -0.26 \pm 0.13$ (c-quark fit). The results are summarized in Table 8. They are consistent with the four-parameter fit.

Table 8: Summary of $R_{q\bar{q}}$ and A_{FB}^q .

| fitting method | flavor | $R_{q\bar{q}}$ | A_{FB}^q | $\chi^2/D.O.F$ |
|----------------------------|---------|-----------------|---------------------------------|----------------|
| four-parameter fit | c-quark | 0.36 ± 0.05 | -0.17 ± 0.14 | 14.93/18 |
| | b-quark | 0.13 ± 0.02 | -0.20 ± 0.16 | |
| 1 quark parameter fit | c-quark | 0.36 ± 0.03 | -0.26 ± 0.13 | 19.29/20 |
| | b-quark | 0.15 ± 0.01 | -0.29 ± 0.13 | 19.29/20 |
| Standard Model predictions | c-quark | 0.30 | -0.48 | |
| | b-quark | 0.13 | -0.43 (mixing $\chi_B = 12\%$) | |

The errors are statistical only.

The differential cross sections for b-quark production ($d\sigma_{b\bar{b}}/d\cos\theta$) and c-quark production ($d\sigma_{c\bar{c}}/d\cos\theta$) were obtained from the $\cos\theta_{thrust}$ distribution. In order to derive $d\sigma_{b\bar{b}}/d\cos\theta$, the contributions from light quarks and $c\bar{c}$ were subtracted, and $b\bar{b}$ was subtracted for $d\sigma_{c\bar{c}}/d\cos\theta$. The results are given in Table 9 and Figure 10. The measured asymmetry for the c- and b-quarks are smaller than the standard-model prediction by 2.2σ and 1.5σ , respectively.

Figure 11 shows the measured $R_{c\bar{c}}$ and $R_{b\bar{b}}$ together with the other experimental data(27; 31; 32). The measured asymmetries of b and c-quark are shown in Figure 12 with the other experimental data(2; 4; 27; 33; 34; 35; 36; 37; 38; 39; 40; 41; 42; 43; 44; 45; 46; 47; 48; 49; 50; 51). The asymmetries measured at PEP(36; 37; 38; 39; 40; 41; 42), PETRA(43; 44; 45; 46; 47; 48; 49; 50; 51), and LEP(27) are combined for each experiment. We combined the present results of A_{FB}^q with our previous measurement by inclusive electron (for c and b quark) and $D^{*\pm}$ (for c quark). The combined values are $A_{FB}^b = -0.28 \pm 0.15$, $A_{FB}^c = -0.35 \pm 0.09$. The combined results are also shown in Figure 12.

6 Conclusion

We have studied inclusive muon events and extracted the cross-sections and charge asymmetries of b and c-quark using all of the data collected with the TOPAZ detector at $\sqrt{s} = 58$ GeV. A total of 1,328 inclusive muon events were selected from 29,561 hadronic events with an integrated luminosity of 273 pb^{-1} . To improve the accuracy of the simulation for pion punch-throughs, we tuned the parameters in the Monte-Carlo simulation, using 1,202 pions from $\tau^\pm \rightarrow \pi^\pm \pi^\pm \pi^\mp \nu$, and $\tau^\pm \rightarrow \rho^\pm \nu$, $\rho^\pm \rightarrow \pi^\pm \pi^0$ in $e^+e^- \rightarrow \tau^+\tau^-$ reaction. The measured ratio, $R_{q\bar{q}}$, of the cross section

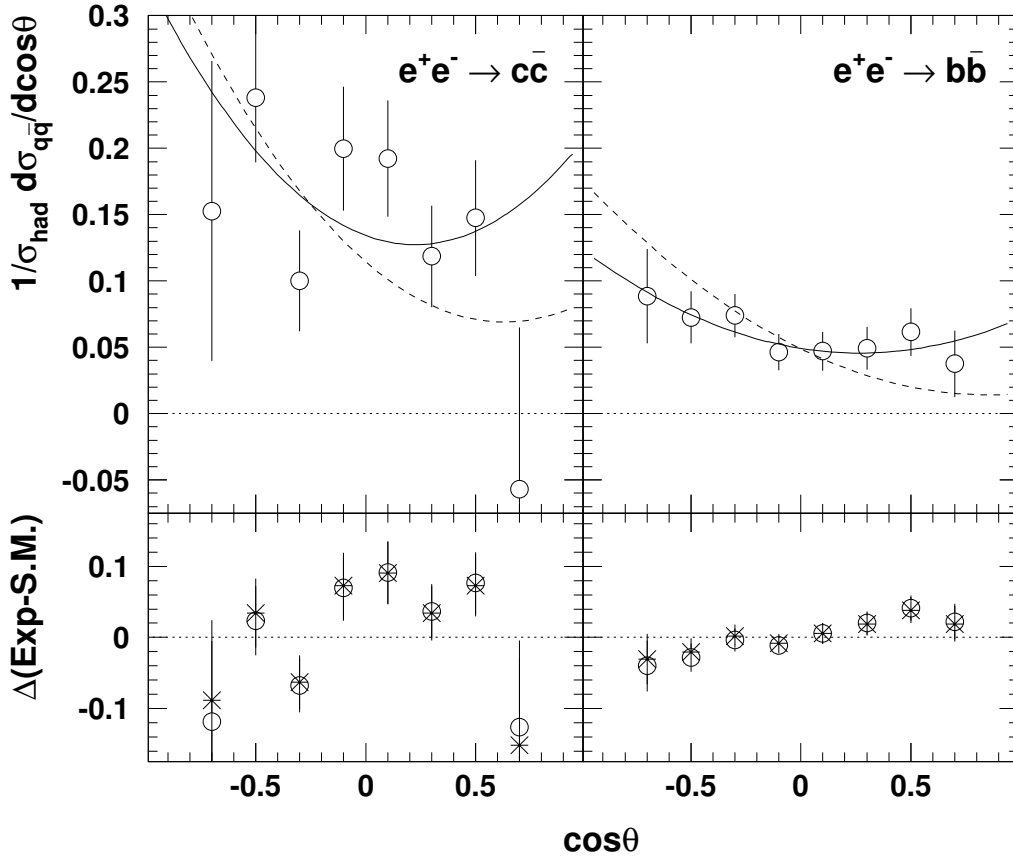


Figure 10: Differential cross section of $e^+e^- \rightarrow b\bar{b}$ and $e^+e^- \rightarrow c\bar{c}$ (upper figures). The solid lines are the best fits and the dashed lines are the standard model predictions. Lower figures show the difference between the observed cross section and the standard model prediction. The open circles are the result of the four-parameter fit and the cross marks are the result of the 1-quark parameter fit.

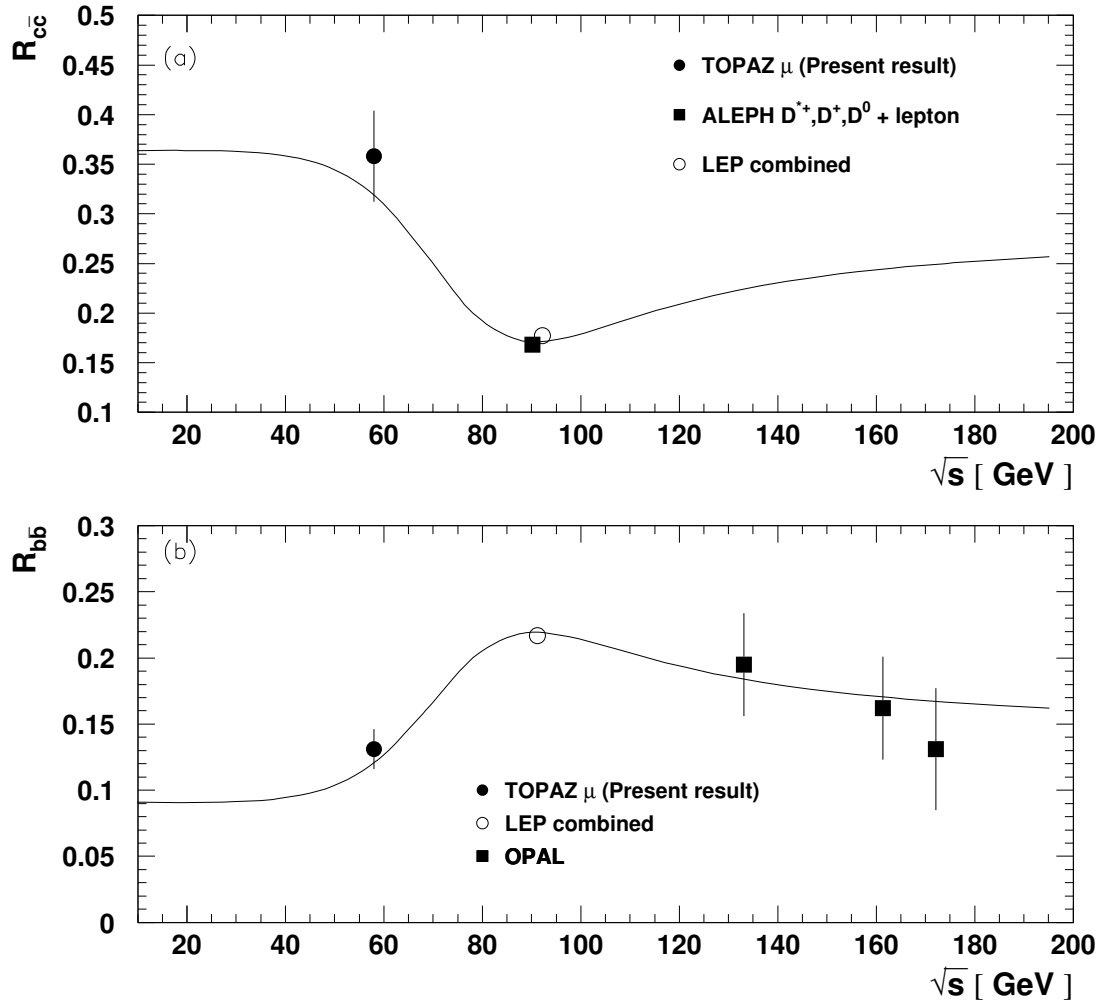


Figure 11: $R_{c\bar{c}}$ (a) and $R_{b\bar{b}}$ (b) as a function of the center-of-mass energy.

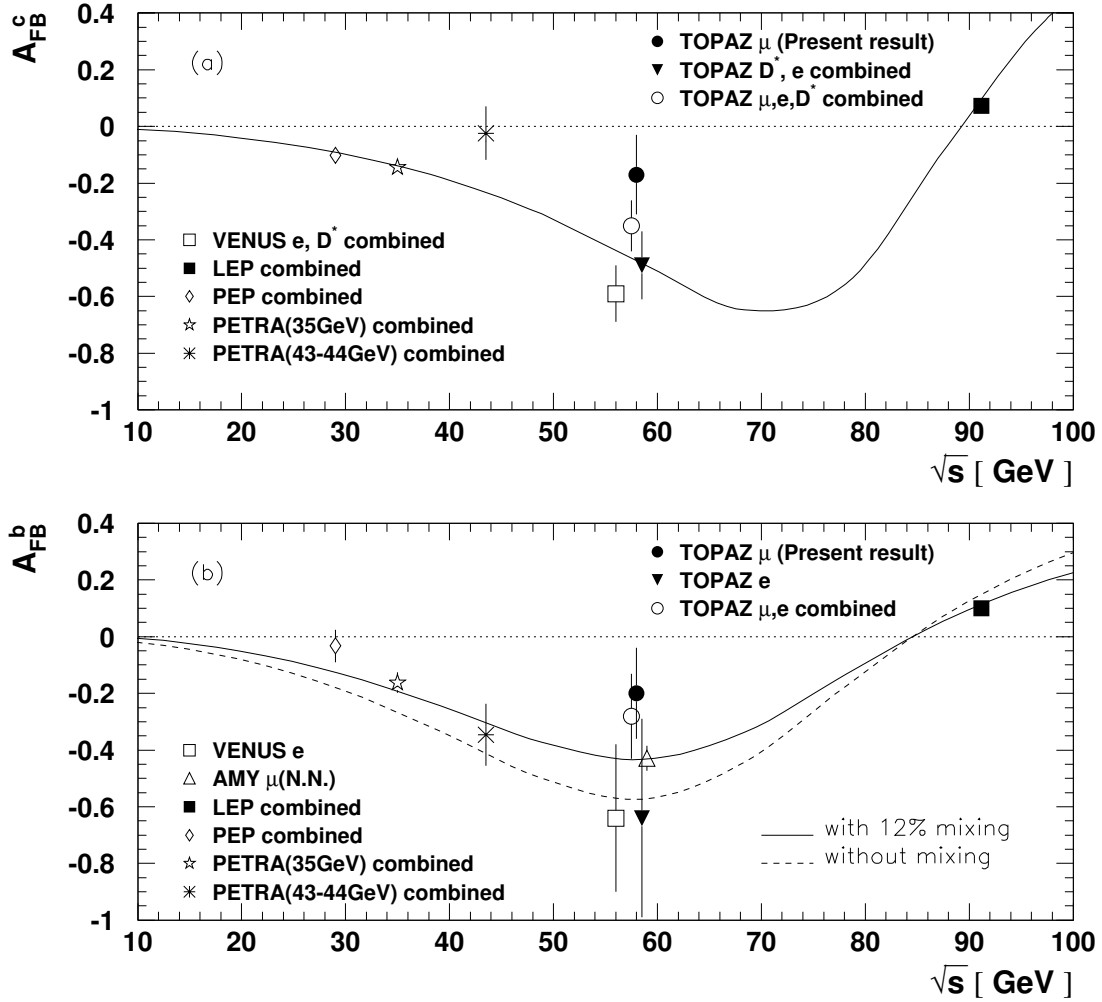


Figure 12: Forward-backward charge asymmetry for c-quark (a) and b-quark (b) as a function of the center-of-mass energy.

Table 9: Differential cross sections for $e^+e^- \rightarrow c\bar{c}$ and $b\bar{b}$ processes.

| $\cos\theta$ bin | $\frac{1}{\sigma_{had}} \frac{d\sigma_{c\bar{c}}}{d\cos\theta}$ | $\frac{1}{\sigma_{had}} \frac{d\sigma_{b\bar{b}}}{d\cos\theta}$ |
|------------------|---|---|
| -0.8 \sim -0.6 | 0.153 \pm 0.113 | 0.088 \pm 0.036 |
| -0.6 \sim -0.4 | 0.238 \pm 0.049 | 0.073 \pm 0.020 |
| -0.4 \sim -0.2 | 0.101 \pm 0.038 | 0.074 \pm 0.016 |
| -0.2 \sim 0.0 | 0.200 \pm 0.047 | 0.046 \pm 0.014 |
| 0.0 \sim 0.2 | 0.192 \pm 0.044 | 0.047 \pm 0.015 |
| 0.2 \sim 0.4 | 0.119 \pm 0.036 | 0.038 \pm 0.016 |
| 0.4 \sim 0.6 | 0.148 \pm 0.044 | 0.062 \pm 0.018 |
| 0.6 \sim 0.8 | -0.057 \pm 0.122 | 0.037 \pm 0.025 |

for $q\bar{q}$ production to the total hadronic cross section and the forward-backward asymmetry, A_{FB}^q , of b and c quark are $R_{b\bar{b}} = 0.13 \pm 0.02(stat) \pm 0.01(syst)$, $R_{c\bar{c}} = 0.36 \pm 0.05(stat) \pm 0.05(syst)$, $A_{FB}^b = -0.20 \pm 0.16(stat) \pm 0.01(syst)$ and $A_{FB}^c = -0.17 \pm 0.14(stat) \pm 0.02(syst)$, respectively. The standard-model prediction for those parameters with 12% $B - \bar{B}$ mixing (χ_B) are $R_{b\bar{b}} = 0.13$, $R_{c\bar{c}} = 0.30$, $A_{FB}^b = -0.43$, $A_{FB}^c = -0.48$, respectively. The measured $R_{b\bar{b}}$ and $R_{c\bar{c}}$ agree with the standard-model predictions, though the measured A_{FB}^b and A_{FB}^c are smaller by 2.2σ and 1.5σ , respectively.

Acknowledgments.

We wish to express our deep thanks to the TRISTAN accelerator group for operating the TRISTAN accelerator excellently for more than eight years. We are grateful to all of the engineers and technicians at KEK and the other collaborating institutions: H. Inoue, N. Kimura, K. Shiino, M. Tanaka, K. Tsukada, N. Ujiie, and H. Yamaoka.

References

- [1] TOPAZ Collaboration, A.Shimonaka et al., Phys. Lett. **B268** (1991) 457.
- [2] TOPAZ Collaboration, E.Nakano et al., Phys. Lett. **B340** (1994) 135.
- [3] TOPAZ Collaboration, K.Nagai et al., Phys. Lett. **B278** (1992) 506.
- [4] TOPAZ Collaboration, E.Nakano et al., Phys. Lett. **B314** (1993) 471.
- [5] M.Kobayashi et al., Nucl. Instr. and Meth. **A312** (1992) 440.
- [6] K.Kamae et al., Nucl. Instr. and Meth. **A252** (1986) 423.
- [7] A.Yamamoto et al., JPN. J. Appl. Phys. **25** (1986) L440.
- [8] T.Kishida et al., Nucl. Instr. and Meth. **A254** (1987) 367.
- [9] S.Kawabata et al., Nucl. Instr. and Meth. **A270** (1988) 11.
- [10] K.Fujii et al., Nucl. Instr. and Meth. **A236** (1985) 55.
- [11] J.Fujimoto et al., Nucl. Instr. and Meth. **A256** (1987) 449.
- [12] H.Hayashii et al., Nucl. Instr. and Meth. **A316** (1992) 202.
- [13] Y.Inoue et al., Nucl. Instr. and Meth. **A385** (1997) 248.
- [14] R.Enomoto et al., Nucl. Instr. and Meth. **A269** (1988) 507.
- [15] T.Tsukamoto et al., Nucl. Instr. and Meth. **A297** (1990) 148.
- [16] N.Ujiie et al., Nucl. Instr. and Meth. **A371** (1996) 421.
- [17] I.Adachi et al., Phys. Lett. **B225** (1991) 613.
- [18] S.Kawabata, Comp. Phys. Comm. **41** (1986) 127.
- [19] T.Sjöstrand, Comp. Phys. Comm. **82** (1994) 74.
- [20] T.Sjöstrand, CERN-TH-6488-92.
- [21] TOPAZ Collaboration, Y.Ohnishi et al., Phys.Lett. **B313** (1993) 475.
- [22] C.Peterson et al., Phys. Rev. **D27** (1983) 105.
- [23] Particle Data Group, R.M.Barnett et al., *Review of Particle Physics*, Phys. Rev. **D54** (1996).
- [24] W.R.Nelson, H.Hirayama, W.O.Roger, SLAC-265, December, 1985.
- [25] H.Fesefeldt, "The Simulation of Hadron Showers-Physics and Applications", PITHA 85/02.
- [26] JADE Collaboration, W.Bartel et al., Z.Phys. **C33** (1986) 23.
- [27] C.Caso et al. (Particle Data Group) *Review of Particle Properties*, Eur. Phys. J. **C3** (1998) 571.
- [28] ALEPH Collaboration, D.Buskulic et al., Phys. Lett. **B343** (1995) 444.
- [29] OPAL Collaboration, G.Abbiendi et al., Eur. Phys. J. **C8** (1999) 573.

- [30] CLEO Collaboration, T.E.Coan et. al., Phys. Rev. Lett. **80** (1998) 1150.
- [31] ALEPH Collaboration, R.Barate et. al., Eur. Phys. J. **C4** (1998) 557.
- [32] OPAL Collaboration, K.Ackerstaff et al., Eur. Phys. J. **C2** (1998) 441.
- [33] AMY Collaboration, K.Ueno et al., Phys.Lett. **B381** (1996) 365.
- [34] VENUS Collaboration, H.Hinode et al., Phys. Lett. **B313** (1993) 245.
- [35] VENUS Collaboration, K.Abe et al., Phys. Lett. **B313** (1993) 288.
- [36] TPC Collaboration, H.Aihara et al., Phys. Rev. **D31** (1985) 2719.
- [37] TPC Collaboration, H.Aihara et al., Z.Phys. **C27** (1985) 39.
- [38] TPC Collaboration, H.Aihara et al., Phys. Rev. **D34** (1986) 1945.
- [39] HRS Collaboration, M.Derrick et al., Phys. Lett. **B146** (1984) 261.
- [40] HRS Collaboration, P.Baringer et al., Phys. Lett. **B206** (1988) 551.
- [41] HRS Collaboration, C.R.Ng et al., ANL-HEP-PR-88-11 (1988).
- [42] MAC Collaboration, H.R.Band et al., Phys. Lett. **B218**(1989) 369.
- [43] JADE Collaboration, W.Bartel et al., Phys. Lett. **B146**(1984) 121.
- [44] JADE Collaboration, F.Ould-Saada et al., Z.Phys. **C44** (1989) 567.
- [45] JADE Collaboration, E.Elsen et al., Z.Phys. **C46** (1990) 349.
- [46] TASSO Collaboration, M.Althoff et al., Phys. Lett. **B126** (1983) 493.
- [47] TASSO Collaboration, M.Althoff et al., Z.Phys. **C22** (1984) 219;.
- [48] TASSO Collaboration, M.Althoff et al., Phys. Lett. **B146** (1984) 443.
- [49] TASSO Collaboration, W.Braunschweig et al., Z.Phys. **C48** (1990) 433.
- [50] CELLO Collaboration, H.J.Behrend et al., Z.Phys. **C47** (1990) 333.
- [51] MarkJ Collaboration, B.Adeva et al., Phys. Rep C. **109** (1989) 131.